

Atypical antiferromagnetic ordering in single crystalline quasi-2D honeycomb magnet YbI_3

Nashra Pistawala,¹ Luminata Harnagea,² Sitaram Ramakrishnan,^{1,2}
Priyanshi Tiwari,³ M. P. Saravanan,³ Rajeev Rawat,³ and Surjeet Singh^{1,*}

¹Department of Physics, Indian Institute of Science Education and Research, Pune 411008, Maharashtra, India

²I-HUB Quantum Technology Foundation, Indian Institute of Science Education and Research, Pune 411008, India

³UGC-DAE Consortium for Scientific Research, University Campus,
Khandwa Road, Indore 452001, Madhya Pradesh, India

(Dated: July 3, 2024)

Here, we study YbI_3 , a quasi-2D layered material with Yb atoms arranged on an ideal honeycomb network of edge-sharing YbI_6 octahedra, analogous to the low-temperature phase of $\alpha\text{-RuCl}_3$. High quality single crystals of YbI_3 are grown from Yb and I as starting precursors, using the vapor transport technique. The grown crystals are characterized by single crystal x-ray diffraction, Raman spectroscopy, magnetization, and heat capacity probes. The crystal-field split ground state of Yb^{3+} in YbI_3 is a well-isolated Kramers doublet with an effective moment $J_{\text{eff}} = 1/2$. Upon cooling, the low-temperature heat capacity of YbI_3 reveals a broad peak at $T_1 = 0.95$ K due to short-range ordering of the Yb moments, followed by a sharp peak at $T_2 = T_N = 0.6$ K due to long-range ordering. The magnetic behavior is found to be weakly anisotropic with $\chi^{\parallel} > \chi^{\perp}$, where χ^{\parallel} and χ^{\perp} refers to the in-plane ($H \parallel ab$) and out-of-plane ($H \perp ab$) susceptibilities. The 2 K isothermal magnetization saturates at $\approx 1.5 \mu_B/\text{Yb}^{3+}$ (in-plane) and $\approx 1 \mu_B/\text{Yb}^{3+}$ (out-of-plane), suggesting the anisotropy to be easy-plane type. The low-temperature heat capacity, well below T_N , is found to vary as T^{α} with $\alpha \approx 2.5$, indicating a possible unconventional magnetic ground state for YbI_3 .

I. INTRODUCTION

Quantum magnetism is one of the frontier areas in condensed matter physics, showcasing unusual ground states, such as, spin liquids with emergent quasiparticles, and exotic spin textures driven by competing interactions [1, 2]. The magnetic interactions in these systems are generally frustrated, which prevents simple, ordered spin arrangements, leading to complex or unconventional ground states. The spin systems based on triangular, Kagome, or pyrochlore lattices are model geometrically frustrated systems, where the competing interactions result from the lattice geometry which does not allow all the nearest-neighbor couplings to be simultaneously satisfied.

The Kitaev model, introduced by Alexei Kitaev in the year 2006 [3], opened-up a new frontier for exploring magnetic frustration. This groundbreaking theoretical framework describes a spin-1/2 system on a two-dimensional honeycomb lattice, where the bond-dependent nearest-neighbor couplings give rise to a strong frustration. The ground state of Kitaev model is a novel quantum spin liquid with Majorana fermions as quasiparticle excitations.

The quest for experimental realization of Kitaev model gained momentum following the seminal work by Jackeli and Khaliullin [4], who laid out a roadmap for uncovering potential Kitaev candidates among the spin-orbit-assisted Mott insulators, specifically the $4d^5$ ruthenates and $5d^5$ iridates. In these compounds, the complex interplay between the strong spin-orbit coupling, octahedral crystal electric field splitting, and electronic correlations give rise to a $J_{\text{eff}} = 1/2$ Kramers doublet ground state with highly anisotropic bond-dependent interactions, which serves as a prerequisite for realizing the Kitaev model.

The electronic and magnetic properties of candidate materials, including, Na_2IrO_3 [5–7], $\alpha\text{-Li}_2\text{IrO}_3$ [8, 9], $\beta\text{-Li}_2\text{IrO}_3$ [10, 11], $\gamma\text{-Li}_2\text{IrO}_3$ [12], $\text{H}_3\text{LiIr}_2\text{O}_6$ [13], Cu_2IrO_3 [14], $\text{Cu}_3\text{LiIr}_2\text{O}_6$ [15], $\text{Ag}_3\text{LiIr}_2\text{O}_6$ [16], $\alpha\text{-RuCl}_3$ [17–23] has been extensively studied in recent years to explore the manifestations of Kitaev physics.

The f -electron systems, based on the rare-earths with $J_{\text{eff}} = 1/2$ Kramer's doublet ground state and edge-shared octahedra have also been theoretically predicted to host Kitaev physics [24–27]. However, suitable materials embodying this concept remain sparse. Xing *et al.* recently investigated the crystal growth and magnetic properties of YbCl_3 , aiming to explore its potential for Kitaev physics [28]. YbCl_3 is a two-dimensional van der Waals material, where the Yb atoms form a slightly distorted honeycomb net, where each Yb atom has nearest-neighbors at 3.886 Å and 3.864 Å [29]. The previous studies reveal short-range ordering of Yb^{3+} moments ($J_{\text{eff}} = 1/2$) around 1.2 K and a Néel-type antiferromagnetic long-range order at 0.6 K, with Yb spins antiferromagnetically aligned within each honeycomb plane, pointing primarily along the a -axis with a small tilt of $\sim 5^\circ$ along the c -axis [28, 30, 31].

A recent study by Matsumoto *et al.* provides evidence for Bose-Einstein condensation in YbCl_3 . When the magnetic field is aligned parallel to the a -axis, YbCl_3 has been argued to undergo a transition from Heisenberg to XY-like state, ultimately achieving a field-polarized state at $H_s = 5.93$ T, marked as the quantum critical point. Upon reducing the field slightly below H_s , YbCl_3 allegedly behaves as a two-dimensional gas of bosons, showing signatures of Bose-Einstein condensation possibly stabilized by a small but non zero interlayer interaction ($\Lambda_{\perp} \approx 0.1$ mK and $\Lambda_{\parallel} \approx 5$ K, where Λ_{\perp} and Λ_{\parallel} are interlayer and intralayer nearest neighbor interactions) [32]. Hence, YbCl_3 is posited as an exemplary two-dimensional system for studying quantum magnetism on a honeycomb lattice.

* email:surjeet.singh@iiserpune.ac.in

Conversely, YbBr_3 , also comprising $J_{\text{eff}} = 1/2$ Heisenberg spins on a honeycomb lattice, demonstrates no long-range ordering down to 100 mK. Based on their inelastic neutron scattering data, Wessler *et al.* argued that despite lacking Kitaev-type anisotropic interactions, YbBr_3 exhibits pronounced quantum fluctuations, perhaps signature of a quantum spin liquid ground state [33]. Considering the novel magnetic behavior associated with the YbCl_3 and YbBr_3 , we set out to investigate the previously unexplored member YbI_3 of this family.

Here, we report the crystal growth of a new two-dimensional van der Waals material, YbI_3 , using the vapor transport technique. YbI_3 crystallizes in $R\bar{3}$ symmetry, determined using the single crystal x-ray diffraction. In this structure, the Yb^{3+} ions form an ideal honeycomb network, with equidistant nearest neighbors with the honeycomb plane. This structure is analogous to the low-temperature ($T < 150$ K) phase of $\alpha\text{-RuCl}_3$, suggesting that YbI_3 is a possible candidate material for studying Kitaev physics.

The ground state of Yb^{3+} in YbI_3 is shown to be a well-isolated Kramers doublet with an effective moment, $J_{\text{eff}} = 1/2$. The magnetic behavior is found to be slightly anisotropic. While the in-plane saturation moment at 2 K is $\approx 1.5 \mu_B/\text{Yb}^{3+}$, it is $\approx 1 \mu_B/\text{Yb}^{3+}$ for the out-of-plane orientation, suggesting an easy-plane behavior analogous to YbCl_3 (here in-plane and out-of-plane refers to the orientation of the applied field with respect to the *ab*-plane). The low-temperature heat capacity shows a broad peak at $T_1 = 0.95$ K due to short-range ordering of the Yb moments, and a sharp peak at $T_2 = 0.6$ K that marks the onset of long-range antiferromagnetic ordering. The value of critical exponent α obtained from fitting the low-temperature heat capacity using the power-law is 2.5, different from $\alpha = 3$ for a 3D Heisenberg antiferromagnets or $\alpha = 2$ for the Heisenberg spins on a 2D lattices, suggesting a possible unconventional quantum ground state for this system.

II. EXPERIMENTAL METHODS

Single crystals of YbI_3 are grown using the vapor transport technique in a two-zone furnace. The details of the crystal growth are given in sec. III A. The x-ray diffraction patterns are recorded using a Bruker D8 advance diffractometer in the Bragg Brentano geometry employing Cu K_α ($\lambda = 1.5406$ Å) radiation. The 2θ values ranged from 5° to 90° with a step size 0.02° . For this purpose, a thin plate-like single crystal was placed over a oven-dried glass-slide and completely covered by a layer of Kapton tape to avoid degradation due to moisture.

Single crystal x-ray diffraction (SCXRD) was carried out using a Bruker Smart Apex Duo diffractometer employing Mo-K_α radiation ($\lambda = 0.70173$ Å) at 250 K and 150 K using an open-flow nitrogen cryostat. A tiny crystal of approximately $1.630 \mu\text{m}$ lateral dimensions was covered in paratone oil to avoid exposure to the atmosphere and mounted on a goniometer loop. The intensities were integrated using the Crystalis Pro [34]. The refinement was performed using Jana

2006 [35].

The layered morphology of the single crystals was confirmed using a scanning electron microscope (SEM) (FEI Make), and the Chemical composition was verified using an Energy Dispersive x-ray (EDX) (Quanta 2003D) detector attached to the SEM instrument in the Secondary Electron (SE) mode. The EDX spectra was collected at 15 – 20 different points, spread across the platelet-shaped single crystal specimen (see the Supplementary Material [36]), to obtain the averaged elemental composition. The elemental mapping was also performed over a micron size area of the single crystal to check the compositional homogeneity of the grown crystal.

Raman spectra were collected at room temperature in the back scattering configuration using a Horiba Jobin-Yvon LabRAM HR spectrometer equipped with liquid nitrogen cooled Charge-Coupled Detector (CCD) and a laser of 532 nm as the source of excitation. The excitation was maintained at 75% of the maximum power, and the accumulation time for each spectrum was 10 s with 30 iterations each time to improve the resolution and intensity of the Raman modes. For the purpose of obtaining Raman spectrum, the YbI_3 crystal was coated with a thin-layer of Apiezon N grease to prevent degradation due the measurement.

Magnetic measurement between 2 – 300 K are performed at the UGC-DAE CSR, Indore using the VSM probe in a Physics Property Measurement System (PPMS), Quantum design, USA. The heat capacity was measured 0.11 K to 4 K using a dilution insert in the PPMS at UGC-DAE-CSR, Indore. Due to highly hygroscopic nature of YbI_3 , the crystal was covered with an unknown amount of Apiezon N grease, hence the addenda could not be measured accurately. However, in the temperature range of our measurement, the magnetic specific heat of YbI_3 is 3 – 4 orders of magnitude higher than that of the Apiezon N grease, and can therefore be safely ignored while analyzing the measured data.

III. RESULTS AND DISCUSSION

A. Crystal growth of YbI_3

High-quality single crystals of YbI_3 are grown using the physical vapor transport (self-transport) technique. Ytterbium powder (99.9% REO, Alfa Aesar) and Iodine flakes (ACS reagent, $\geq 99.8\%$, Sigma Aldrich) are used in their elemental form as starting precursors. The stoichiometric quantities of the starting materials are loaded in a quartz ampoule, measuring approximately 15 cm in length, with an inner diameter of about 2 cm and wall-thickness of 2 mm, resulting in a volume of around $40 - 50 \text{ cm}^3$. To compensate for iodine sublimation losses during the evacuation process, an additional 10% excess of iodine is included. The entire procedure of handling and storing the precursors is carried in an argon-filled glove box with oxygen and moisture content < 0.1 ppm. Before loading the precursors into the ampule, thorough cleaning steps are undertaken. The ampule undergoes sonication in acetone, followed by rinsing with deionized water. Subsequently, it is preheated to 1000°C to elim-

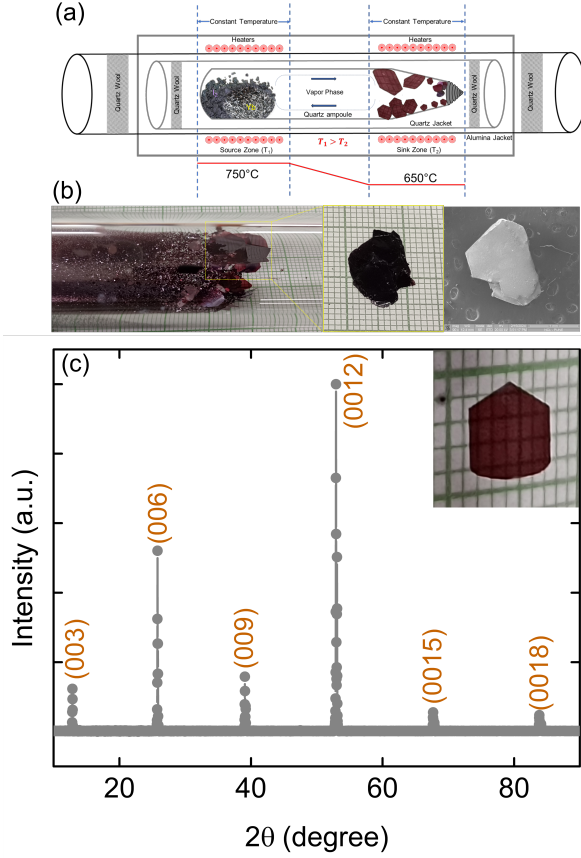


FIG. 1. (a) Schematic of vapor transport reaction for YbI_3 in a sealed quartz ampoule kept in a temperature gradient furnace. (b) Actual growth ampoule (left), containing several small crystals, and a large cm-sized single crystal (middle). A scanning electron microscope image of a small crystal specimen used for chemical analysis (right). (c) x-ray diffraction was conducted in Bragg Brentano geometry, displaying the $(0\ 0\ l)$ reflections which confirms the ab -plane of the single crystal specimen shown in the inset.

inate residual moisture and organic impurities sticking to its inner walls. The filled ampoule is evacuated down to 10^{-5} torr, and thereafter flame-sealed under dynamic vacuum. Given iodine's high vapor pressure at room temperature (approximately 100 Pa at 309 K), the ampoule was kept under an ice bath during evacuation and sealing to minimize iodine losses. The sealed ampoule is then kept in a two-zone furnace under a temperature gradient $\Delta T = 100^\circ\text{C}$, with the source temperature set at 750°C (T_{source}) and the sink temperature (T_{sink}) at 650°C . The schematic of vapor transporter reaction is shown in Fig. 1(a). Optimal growth conditions for producing the largest and highest quality single crystals involve simultaneous cooling of both the zones at a rate of 0.3°C h^{-1} down to $T_{\text{source}} = 600^\circ\text{C}$ and $T_{\text{sink}} = 400^\circ\text{C}$. Subsequently, both zones of the furnace are cooled simultaneously to room temperature.

The experiments performed using different growth conditions are summarized in Table S2. (See Supplemental Material) [36]. Shiny, plate-like single crystals, with typical lateral

dimensions of $1\text{ cm} \times 1\text{ cm}$, and dark-brown/transparent appearance, as shown in Fig. 1(b), are obtained. The plate-like morphology of the grown crystals is a reflection of the underlying layered or quasi-two-dimensional structure of YbI_3 . A scanning electron microscope image of a small crystal specimen is shown in Fig. 1(b). The chemical composition, obtained using EDX, confirms the 1:3 ratio of Yb:I (see Fig. S1 and Table S2. of the Supplemental Material) [36].

The x-ray diffraction pattern collected from a plate-like single crystal specimen is shown in Fig. 1(c). The specimen used is shown in the inset. The pattern is collected in the Bragg Brentano geometry, revealed diffraction peaks with miller indices $(00l)$, where $l = 3, 6, \dots$, suggesting that the large lateral surface of the measured specimen is oriented perpendicular to the c -axis.

The crystals are found to be extremely hygroscopic, decomposing into white powder and eventually into a liquid droplet when exposed to the ambient atmosphere. Therefore, due care is required during sample preparation and while loading the sample for measurements in a cryostat as described in Sec. II.

B. Crystal Structure

The symmetry of YbI_3 was found to be trigonal $R\bar{3}$ (# 148) from single crystal x-ray diffraction, which is in agreement with the L Asprey et al.[37]. Temperature-dependent single crystal x-ray diffraction measurements at 250 K and 150 K show an absence of structural transition and that the symmetry remains trigonal as shown in Fig. S2. (see Supplemental Material) [36], unlike $\alpha - \text{RuCl}_3$, which exhibits a change of symmetry from room-temperature monoclinic ($C2/m$) to low-temperature trigonal ($R\bar{3}$) symmetry below a temperature of 150 K [38]. The symmetry of the lattice is further substantiated by the reciprocal space cuts shown

Crystal structure of YbI_3 in the ab -plane is shown in Fig. 2(a), illustrating the honeycomb network of Yb atoms similar to $\alpha\text{-RuCl}_3$ [39] and YbBr_3 [33]. Each Yb atom is coordinated to six neighboring I atoms in an almost ideal edge-sharing octahedral arrangement. In the honeycomb layer, the Yb-Yb bond distance is $4.226(1)\text{ \AA}$, while the distance along the c -axis is $6.803(4)\text{ \AA}$ as shown in Fig. 2(c), where the stacking of the honeycomb layers perpendicular to the c -axis can be seen. The Yb-I-Yb bond angle in the honeycomb layer is $91.76(3)^\circ$ (see panel (e) in Fig. 2). The octaheron of ligands I atoms around the central Yb atom is shown in Fig. 2(g).

The details of the data collection strategy, crystallographic information and refinement parameters are summarized in Table I. The atomic positions with their corresponding isotropic displacement parameters (ADPs) are listed in Table II.

The crystal structure of YbI_3 is different from YbCl_3 , where the later crystallizes with a monoclinic $C2/m$ crystal structure [28, 29], analogous to the room-temperature phase of $\alpha\text{-RuCl}_3$. However, unlike $\alpha\text{-RuCl}_3$, which undergoes a structural phase transition to $R\bar{3}$ symmetry below 150 K, YbCl_3 remains in the $C2/m$ symmetry over the whole temperature range. In $C2/m$ symmetry, the hexagonal ring of the Yb atoms is not perfect with two different Yb-Yb bond

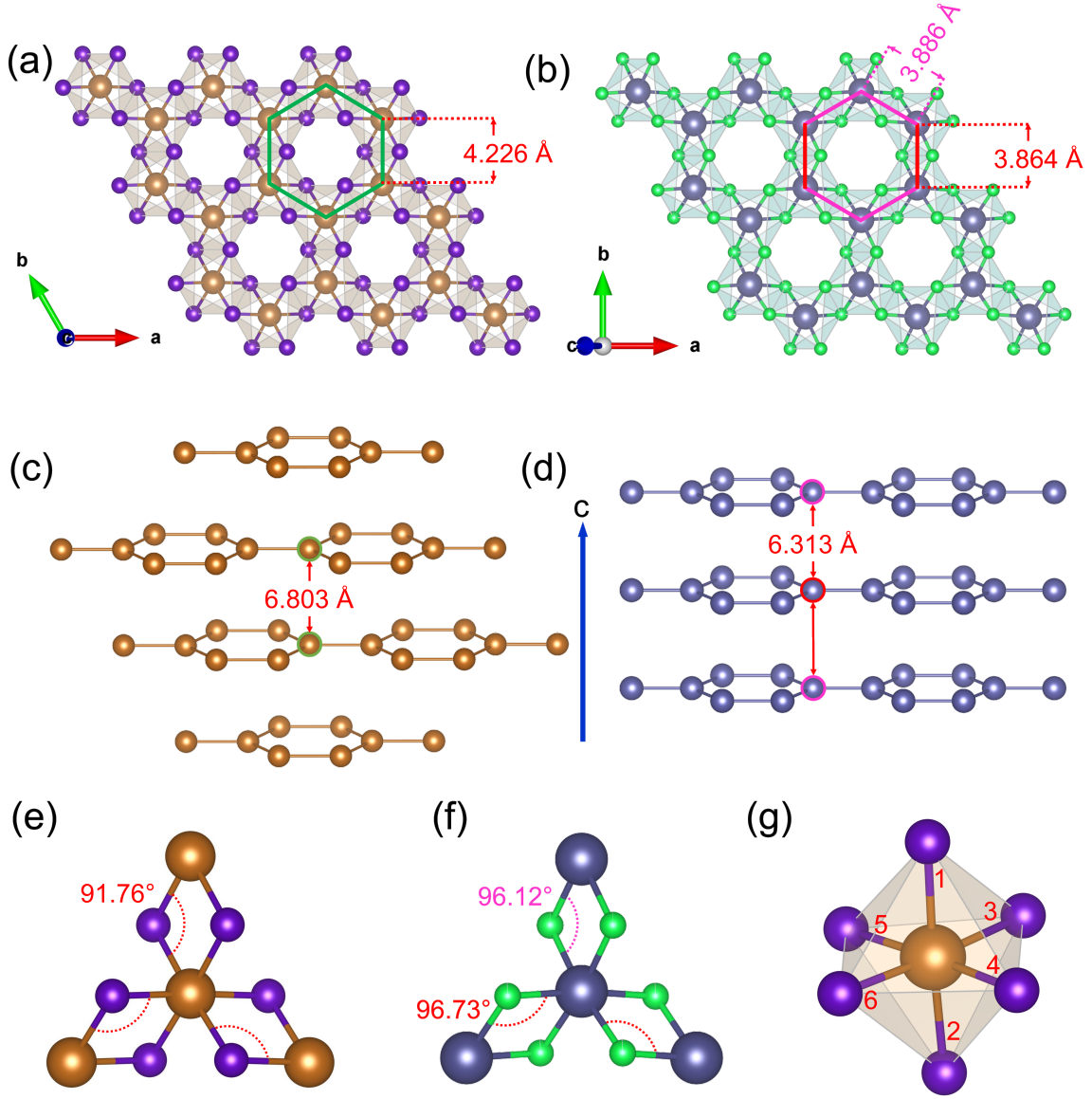


FIG. 2. Crystal structure of YbI₃. (a) Projection of the *ab*-plane showing the arrangement of Yb ions on a honeycomb lattice. The hexagonal rings formed by the Yb atoms, exemplified using green solid lines, is regular with each side 4.226(1) Å. (b) Analogous image for YbCl₃ is shown for comparison. In this case the hexagonal ring is slightly distorted with Yb-Yb distances 3.886 Å and 3.864 Å [29]. (c) Stacking of the honeycomb layers of YbI₃ perpendicular to the *c*-axis. The nearest neighbor Yb-Yb distance along the *c*-axis is 6.803(4) Å. (d) Analogous image for YbCl₃ is shown for comparison, where the nearest neighbor Yb-Yb separation is 6.313 Å [29]. (e) and (f) comparison of Yb-I-Yb bond angles along the three nearest neighbors in the *ab*-plane. These angles are uniformly 91.76(3)° in YbI₃, and 96.12° and 96.73° in YbCl₃ [29]. (g) A regular octahedron of I atoms around the Yb atom. Each Yb-I bond distance is close to 2.942(3) Å.

distances of 3.886 Å and 3.864 Å. The Yb-Cl-Yb bond angles also take two different values, namely 96.12° and 96.73°, thus lacking the C_3 symmetry [29]. The effect of symmetry breaking has been discussed in the recent study by Kim et. al [40]. The C_3 symmetry with 90° bond angles and larger inter-layer separation along the *c*-axis are ideal criteria for realizing the Kitaev model [41], which minimizes the Heisenberg interaction, allowing Kitaev interactions to dominate, as shown in the case of α -RuCl₃ [39, 42]. As mentioned above, YbCl₃

has a slightly distorted honeycomb net with different bond angles and with more number of nearest neighbors along the *c*-axis [29]. YbBr₃, on the other hand, has a similar structure as that of YbI₃ and low-temperature phase of α -RuCl₃ but with small site-disorder on the Yb site [33]. To summarize, between the three Yb based halides compared here, YbI₃ appears to have the closest resemblance to the low-temperature phase of α -RuCl₃.

TABLE I. Crystallographic data and refinement parameters for SCXRD of YbI₃ single crystal at 250 K.

Temperature (K)	250
Crystal system	Trigonal
Lattice system/Setting	Hexagonal
Space group (Point group)	$R\bar{3} (C_{3i}^2)$
No.	148
a (Å)	7.3201(8)
c (Å)	20.4545(27)
Volume (Å ³)	949.2(3)
Z	6
Wavelength (Å)	0.71073
Detector distance (mm)	40
Scan type	Full sphere (ϕ, ω scans)
Rotation per image (deg)	0.8
Exposure time (sec)	10
$(\sin(\Theta)/\lambda)_{max}$ (Å ⁻¹)	0.743374
Absorption, μ (mm ⁻¹)	29.261
T_{min}, T_{max}	0.84, 1.08
Criterion of observability	$I > 3\sigma(I)$
No. of reflections measured	10072
Unique reflections (obs/all)	561/728
R_{int} (obs/all)	0.1022/0.1054
No. of parameters	14
R_F (obs)	0.0556
wR_F (all)	0.0720
GoF (obs/all)	3.98/3.50
$\Delta\rho_{min}, \Delta\rho_{max}$ (e Å ⁻³)	-3.59, 3.77

TABLE II. Atomic Coordinates x, y, z and atomic displacement parameters (ADPs) of YbI₃ single crystal at 250 K in Å². Unique reflections (obs/all) = 561/728, criterion of observability: $I > 3\sigma(I)$, $R_F = 0.0556$, No. of refined parameters = 14, Refinement method used: least-squares on F, Space group: $R\bar{3}$. The complete data including the anisotropic atomic displacement parameters, are shown in Table S3.(see Supplemental Material) [36].

Atoms	Wyck	x	y	z	Occ.	U_{iso}^{eqi}
Yb	6c	0	0	0.3337(4)	1	0.0182(3)
I	18f	0.3229(1)	0.3341(1)	0.4165(1)	1	0.0228(4)

C. Raman Spectroscopy

As discussed above, YbI₃ has a Trigonal symmetry with the point group symmetry C_{3i}^2 . According to the group theory, the irreducible representation of the zone-center Raman active phonon modes in YbI₃ are $\Gamma(C_{3i}^2) = 4A_g + 4^1E_g + 4^2E_g$. However, if the inter-layer coupling is treated as a small correction, the single-layer of YbI₃ has the D_{3d} point group symmetry, rendering six Raman active modes, $\Gamma(D_{3d}) = 4E_g + 2A_{1g}$. Fig. III C shows the observed Raman spectrum for YbI₃ single crystal. The whole spectrum could be nicely fitted using a total of six Lorentzian lineshapes corresponding the six expected Raman active phonon modes. The modes are labeled from P₁ to P₆ in the increasing order of frequency as $\Delta\omega = 38.4$ (P₁), 56.4 (P₂), 69.4 (P₃), 94.0 (P₄), 118.5 (P₅), and

142.5 (P₆) cm⁻¹. The modes P₁, P₃, P₄, and P₆ have the E_g symmetry, whereas symmetry of P₂ and P₅ is A_{1g} . Additionally, four weak modes at 61.6 (M₁), 74.3 (M₂), 114.1 (M₃), and 137.5 (M₄) are also observed. The presence of weak extra modes in the Raman spectrum are not unusual. These are often assigned as infrared active modes rendered Raman active due to lowering of the local symmetry at some sites [43]. In some cases, the extra modes are assigned to second-order Raman scattering [44]. The observed spectrum (including some of the weak extra modes) agrees well with that reported for the isostructural compound DyI₃ [45]. The observed phonon modes for YbI₃ and DyI₃, and their corresponding symmetries in the D_{3d} representation, are listed in Table S4.(see Supplemental Material) [36].

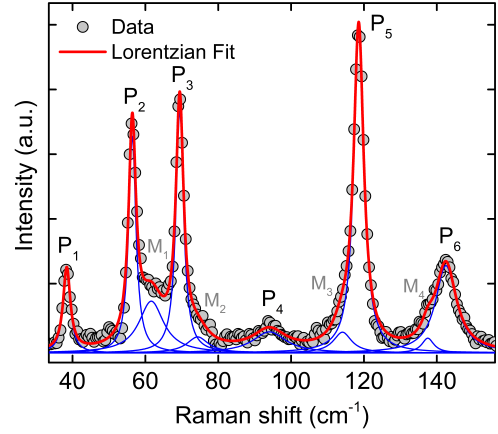


FIG. 3. Raman spectrum of YbI₃ single crystal. The six Raman active phonon modes are labelled from P₁ to P₆.

D. Heat Capacity

Fig. 4(a) shows the heat capacity C_p plotted as C_p/T as a function of temperature from $0.1 \text{ K} \leq T \leq 1.5 \text{ K}$. The heat capacity is an additive quantity, comprising various contributions, and can be expressed as: $C_p(T) = C_{mag} + C_{latt} + C_{nuc}$, where C_{mag} is contribution to heat capacity arising from the $4f$ electrons of Yb³⁺, C_{nuc} is the nuclear Zeeman contribution, and C_{latt} is the lattice contribution. In the temperature range of measurement, the lattice contribution due to phonons becomes extremely small and can therefore be neglected. As shown in Fig. 4(a), the C_p/T exhibits three distinct features at temperatures T_1 , T_2 , and T^* . The broad anomaly around 0.95 K, labeled as T_1 , is attributed to the short-range ordering of the Yb³⁺ moments, whereas the sharp λ -type anomaly at 0.6 K, labeled as T_2 , has been tentatively attributed to their long-range ordering. The upturn below T^* is due to nuclear Zeeman splitting caused by the internal field generated by the ordering of Yb moments [46].

Here, it would be instructive to bring a comparison with much more extensively studied YbCl₃. In case of YbCl₃, a

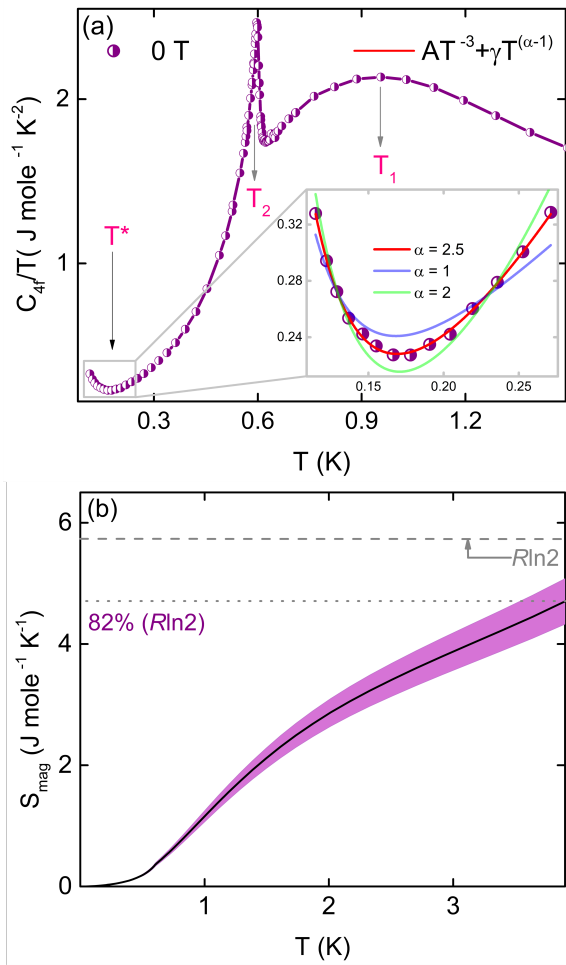


FIG. 4. The temperature variation of heat capacity (C_p) and magnetic entropy released (S_{mag}): (a) C_p/T is shown as a function of temperature. Inset: solid red line is a fit to the low temperature experimental data for $\alpha = 2.5$. The fit using $\alpha = 1, 2$ is also shown for reference (see text for details). (b) S_{mag} is shown as a function of temperature. The purple shaded region indicates the error bars.

similar broad peak attributed to short-range ordering appears at 1.2 K, followed by weaker anomalies at 0.6 K and 0.4 K upon further cooling [28]. While the 0.6 K anomaly is linked to the long-range ordering of the Yb moments, the 0.4 K anomaly is sample-dependent and has been attributed to the presence of defects/imperfections or impurities. In contrast, in the YbI_3 , the peak corresponding to the long-range ordering at $T_2 = 0.6$ K is sharp and well-defined, while the 0.4 K anomaly could not be detected in YbI_3 .

We fitted the heat capacity data of YbI_3 below 0.3 K using the expression: $C_p = AT^{-2} + \gamma T^\alpha$, where the first term in the equation is the high-temperature approximation of the two-level Schottky equation [47], and the second term is written based on the assumption that C_{mag} follows a certain power-law behavior in the ordered state. The data fits well as shown with a red solid curve in the inset of Fig. 4(a). The values obtained for the parameters A , γ and α from the fitting are: $A = 3.67 \times 10^{-4} \text{ J mole}^{-1} \text{ K}$, $\gamma = 2.2 \text{ J mole}^{-1} \text{ K}^{-3.5}$,

and $\alpha = 2.5$. For YbCl_3 , the exponent α is 1.5 [32]. The fit using the $\alpha = 1, 2$ is shown in the inset of Fig. 4(a) using blue and green solid curves, respectively. The fitting clearly indicates that the value of exponent α is 2.5 in case of YbI_3 . In the magnetically ordered state of traditional antiferromagnets, the exponent α is expected to be 3, whereas in the case of layered antiferromagnets the expected value of α should be 2. On the other hand, $\alpha \approx 1$, indicating a linear temperature dependence of low-temperature heat capacity conventionally holds for the spinons in gapless quantum spin liquids; whereas a more unconventional quadratic temperature dependence ($\alpha \approx 2$) is expected for a gapless Dirac fermions [48]. The value of $\alpha \approx 2.5$ in the present case of YbI_3 is possibly an indication of an unusual ground state. Further, experiments in the presence of applied magnetic field, currently not accessible to us, will be illuminating in understanding the ground state of YbI_3 accurately.

Fig. 4(b) shows the magnetic entropy released as a function of temperature calculated using $S_{\text{mag}} = \int_0^{T_0} C_{\text{mag}}(T)/T dT$. We extracted C_{mag} by subtracting the nuclear contribution from the total heat capacity. As mentioned in the beginning (Sec. II), the addenda accounting for the contribution from the Apiezon N grease used for thermal contact and for covering the same to prevent it from decomposing in the process of loading for low-temperature measurements has not been subtracted. However, at low-temperatures, where C_{mag} is overwhelmingly large, we do not expect the Apiezon N contribution to be of much significance. The temperature variation of S_{mag} is shown in Fig. 4(b). Above 0.5 K, S_{mag} rises sharply, tapers a bit around 2 K, but do not show any signs of saturation up to 4 K. At 4 K, the value approaches 82% of $R\ln 2$. Since the measurements were only conducted up to 4 K, the exact temperature at which the magnetic entropy plateaus at $R\ln 2$ is not known. However, previous reports on YbCl_3 [28] suggest that this plateau will possibly occur at a slightly higher temperature (close to 10 K). A value of $S_{\text{mag}} \approx R\ln 2$, shows that the crystal field split ground state of Yb^{3+} in YbI_3 is a Kramer's doublet. To establish this further, we investigated the magnetic behavior of our YbI_3 crystals, discussed next.

E. Magnetization

Magnetic susceptibility (χ) is measured by applying a magnetic field of 10 kOe, in the parallel (χ_{\parallel}) (in-plane) and perpendicular ($\chi_{\perp}(T)$) (out-of-plane) orientations. The temperatures variation of in-plane and out-of-plane susceptibilities are shown in Fig. 5(a). For the out-of-plane orientation, the zero-field-cooled (ZFC) and field-cooled (FC) curves overlap over the whole temperature range, but in the in-plane susceptibility, a very weak splitting is observed below approximately 150 K (not shown).

The high temperature $1/\chi$ data ($150 \leq T \leq 300$) are fitted using a modified Curie-Weiss (CW) expression: $\chi = \chi_0 + C/(T - \Theta_{\text{CW}})$, where C is the Curie-constant from which the value of the effective magnetic moment (μ_{eff}) can be derived using $\mu_{\text{eff}} = \sqrt{8C}$; Θ_{CW} is the Weiss temperature, and χ_0 is a small temperature independent term that usually

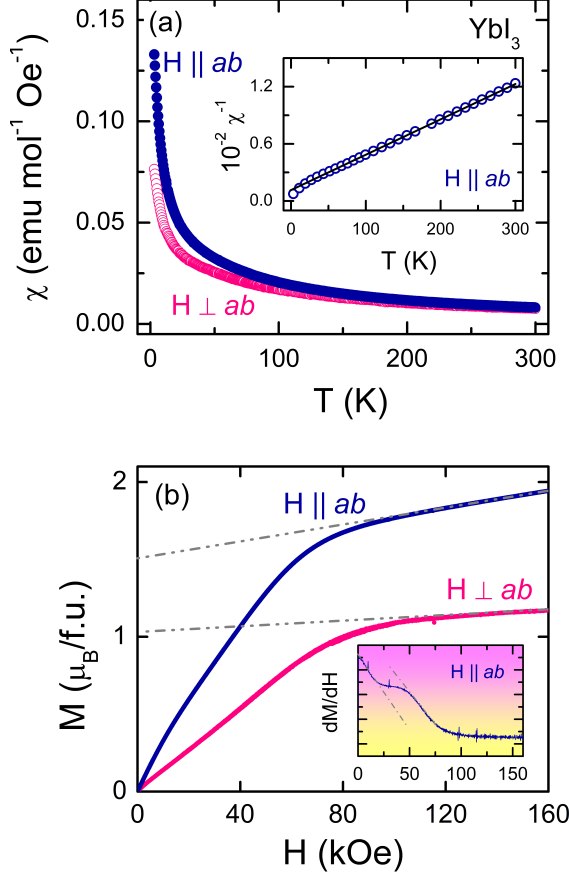


FIG. 5. The magnetic susceptibility (χ) and isothermal magnetization $M(H)$ of YbI_3 : (a) Temperature variation of χ_{\parallel} and χ_{\perp} measured under an applied field magnetic field of 10 KOe. Inset: $\chi^{-1}(T)$ plotted as a function of temperature for $H \parallel ab$. The solid line through the data points in the inset is the modified Curie-Weiss fit (see text for details). (b) $M(H)$ at 2 K for $H \perp ab$ and $H \parallel ab$. The dashed lines represent linear extrapolation of the high-field data to $H = 0$. Inset: derivative dM/dH plot.

arise due to core diamagnetism and/or van Vleck type paramagnetism.

The values of the fitting parameters for the in-plane and out-of-plane orientation are as follows: $\chi_0^{\perp} = 3.8 \times 10^{-4} \text{ emu mole}^{-1} \text{ Oe}^{-1}$, $\Theta_{\text{CW}}^{\perp} = -55 \text{ K}$, and $\mu_{\text{eff}}^{\perp} = 4.53 \mu_{\text{B}}/\text{Yb}^{3+}$; the corresponding values in the in-plane orientation are: $\chi_0^{\parallel} = 1.9 \times 10^{-4} \text{ emu mole}^{-1} \text{ Oe}^{-1}$, $\Theta_{\text{CW}}^{\parallel} = -24 \text{ K}$, and $\mu_{\text{eff}}^{\parallel} = 4.53 \mu_{\text{B}}/\text{Yb}^{3+}$. In both cases, the value of μ_{eff} agrees well with the calculated value of $\mu_{\text{eff}} = g_J \sqrt{J(J+1)} = 4.53 \mu_{\text{B}}$ for Yb^{3+} ($4f^{13}$: $L = 3, S = 1/2$, and $J = 7/2$). The large values of Θ_{CW} for both the orientations are unrealistic, which may be due to the large crystal field splitting of the $J = 7/2$ manifold. In the presence of an octahedral crystal field environment of surrounding I^- ions, the eight-fold degenerate, $J = 7/2$ manifold in a free Yb^{3+} ion will split into four Kramers doublet. As a reference, we note that in YbCl_3 , the four Kramers doublets are located at ener-

gies, 0, 243, 371, and 456 K. Clearly, in the range over which the fitting is performed, the van Vleck contribution from the higher-lying levels will be small but not insignificant.

In such scenarios where the crystal field splitting is large, it is more instructive to fit the low-temperature data to estimate the magnetic moment in the lowest Kramers doublet. We fitted the data in the temperature range from 4 K to 12 K using the modified Curie-Weiss expression. The values of the fitting parameters thus obtained are listed in Table III. For both the orientations, if we fix $\chi_0 = 0$, we get $\mu_{\text{eff}}^{\perp} = 2.8 \mu_{\text{B}}/\text{Yb}^{3+}$, $\mu_{\text{eff}}^{\parallel} = 3.24 \mu_{\text{B}}/\text{Yb}^{3+}$; and, $\Theta_{\text{CW}}^{\perp} = -10 \text{ K}$, $\Theta_{\text{CW}}^{\parallel} = -7 \text{ K}$. In YbCl_3 , the corresponding values are [28]: $\mu_{\text{eff}}^{\perp} = 3.0 \mu_{\text{B}}/\text{Yb}^{3+}$, $\mu_{\text{eff}}^{\parallel} = 3.1 \mu_{\text{B}}/\text{Yb}^{3+}$; and, $\Theta_{\text{CW}}^{\perp} = -9 \text{ K}$, $\Theta_{\text{CW}}^{\parallel} = -6 \text{ K}$. The two sets of values are in good agreement with each other, suggesting some degree of similarity between the two systems. In both cases, the value of Θ_{CW} is somewhat higher than expected as we do not expect the exchange interaction to be of the order of 10 K for the reason that the $4f$ -electrons in rare-earths are highly sequestered, shielded by $5d$ and $6s$ electrons, which prevents them from making an appreciable overlap with the ligand p orbitals. For example, in the Yb-based pyrochlore oxides, the exchange interaction is of the order of 1 K. The other problem with these values is that the estimated Weiss temperature is comparable from the two orientations, which appears improbable given the layered nature of these materials, which suggests that the interaction within the plane should be much stronger than out-of-plane. In YbCl_3 , the in-plane nearest-neighbor coupling strength is $\Lambda_{\parallel} \approx 5 \text{ K}$ and $\Lambda_{\perp}/\Lambda_{\parallel} \approx 10^{-5}$ [31]. The exact reason for the high Weiss temperature in the low-temperature Curie-Weiss fits is not yet clear. Fixing χ_0 to some high value ($\sim 10^{-4} - 10^{-3} \text{ emu mole}^{-1} \text{ Oe}^{-1}$) did not decrease the Weiss temperature significantly either. We believe that the short-range magnetic correlations, that persists up to very high temperatures, may have contributed to the high value of Θ_{CW} . Strong spin fluctuations or short-range correlations are intrinsic to the layered (or quasi-2D) magnets, which is reflected in the broad peak in the heat capacity and a nearly linearly increasing S_{mag} up to temperatures as high as $\sim 7T_N$ (here $T_N = T_2$ corresponds to the sharp anomaly in C_p). The value of anisotropic g -factor in YbI_3 is estimated to be $g_J^{\perp} = 3.2$ and $g_J^{\parallel} = 3.8$, assuming $J_{\text{eff}} = 1/2$. In comparison, from a similar analysis the anisotropic g -factor in YbCl_3 is $g_J^{\perp} = 3.5$ and $g_J^{\parallel} = 3.6$ [28]. Slightly smaller values for the g -factors are obtained by taking χ_0 values from the isothermal magnetization, as discussed below.

Isothermal magnetization, $M(H)$ for out-of-plane ($H \perp ab$) and in-plane ($H \parallel ab$) orientations is shown in Fig. 5 (b). In the out-of-plane orientation, the magnetization nearly saturates above a field of $H \approx 120 \text{ kOe}$. The small slope that still persists can be attributed to the van Vleck term (χ_0), which can be calculated by fitting the high-field data to an expression of the $M = M_s^{\perp} + \chi_0^{\perp} H$, where M_s^{\perp} is the saturation magnetization in the out-plane orientation. The fit, which is shown in the Fig. 5(b) using a dashed line (shown extrapolated to $H = 0$), gives $M_s^{\perp} \approx 1 \mu_{\text{B}}/\text{Yb}^{3+}$ and $\chi_0^{\perp} = 5.6 \times 10^{-3} \text{ emu mol}^{-1} \text{ Oe}^{-1}$. Using these values of χ_0 for

TABLE III. Summary of fitting parameters χ_0 (emu mole⁻¹ Oe⁻¹), C (emu mole⁻¹ Oe⁻¹ K), μ_{eff} (μ_B), anisotropic Lande g-factor and Θ_{CW} (K) obtained by fitting the magnetic susceptibility data for in-plane ($H \parallel ab$) and out-of-plane ($H \perp ab$) orientations

Orientation	Temperature range (K)	χ_0	C	μ_{eff}	g-factor	Θ_{CW}	Ref.
$H \perp ab$	150 – 300	3.82×10^{-4}	2.57	4.53	–	–55	
	4 – 12	0 ^a	0.98	2.80	3.2	–10	This work
	4 – 12	5.5×10^{-3} ^b	0.82	2.56	3.0	–8	
	^c 3 – 15	0	1.12	3.0(1)	3.5(1)	–9	[28]
$H \parallel ab$	150 – 300	1.95×10^{-4}	2.57	4.53	–	–24	
	4 – 12	~ 0 ^a	1.32	3.24	3.8	–7	This work
	4 – 12	16×10^{-3} ^b	0.93	2.73	3.2	–5	
	^c 3 – 15	0	1.20	3.1(1)	3.6(1)	–6	[28]

^a when χ_0 is fixed as 0; ^b When χ_0 is fixed to the value obtained from the slope of the linear-section of the high field isothermal magnetization plots. ^c YbCl₃

the orientations (instead of fixing them to zero, as done in the previous paragraph), we get $g_J^\perp = 3.2$ and $g_J^\parallel = 3.0$ (see Table. III). Combining the two results, we can conclude that the approximate g_J values for the two orientations are: $g_J^\perp \approx 3.0 \pm 0.2$ (out-of-plane), and $g_J^\parallel \approx 3.4 \pm 0.3$ (in-plane).

For the in-plane M(H) a more intriguing field variation is observed, as depicted using the derivative (dM/dH) plot in the inset of Fig. 5(b). With increasing field, dM/dH exhibits a plateau in the field ranging from 20 kOe to 40 kOe, suggesting a field induced transition. In the high-field region dM/dH becomes almost flat and very small. Analyzing the high-field region as before yields: $M_s^\parallel \approx 1.5 \mu_B/\text{Yb}^{3+}$ and $\chi_0^\parallel = 16 \times 10^{-3} \text{ emu mol}^{-1} \text{ Oe}^{-1}$. Using, the g-factor obtained for the two orientations from the susceptibility data, a back calculation of the saturation moment suggests $J_{\text{eff}} \leq 1/2$.

F. YbI₃ versus YbCl₃

To begin with, the crystal structures of YbI₃ and YbCl₃ are distinct from one another. YbI₃ exhibits trigonal symmetry, while YbCl₃ displays monoclinic symmetry [29]. This primary difference is due to the variation in the stacking sequence of YbX₃ layers along the *c*-axis. In YbI₃, three layers form a repeating unit, resulting in nearest neighbor Yb–Yb distance of 6.803 Å along the *c*-axis, as shown in Fig. 2(c). In contrast, YbCl₃ consists of a single layer repeated along the *c*-axis, leading to nearest neighbors at 6.313 Å in the layers above and below the middle layer, as shown in Fig. 2(d). Beyond the global symmetry, the local symmetry within a single YbX₃ layer in the *ab*-plane also differs slightly for the two compound, which may be crucial for understanding the magnetic behavior of these materials. In YbCl₃, the Yb–Yb honeycomb bond distances are 3.886 Å and 3.864 Å; accordingly, the bond angles are 96.12° and 96.73°, respectively [29]. Conversely, YbI₃ features a uniform bond distance of 4.226(1) Å and a bond angle of 91.76(3)°, resulting in an isotropic honeycomb lattice with equal bond distances and angles. Although the distortion in YbCl₃ is very small,

it nevertheless causes the breaking of C₃ symmetry, which is preserved in the case of YbI₃.

Heat capacity measurements reveal two distinct transitions in both compounds. In YbI₃, short-range ordering occurs at 0.95 K, followed by long-range ordering at 0.6 K. Similarly, in YbCl₃, short-range ordering occurs at 1.2 K, followed by long-range ordering at 0.6 K. The entropy release for both compounds approaches $R \ln 2$, indicating a $J_{\text{eff}} = 1/2$ Kramers doublet ground state. Regarding differences, the transition at 0.6 K attributed to the long-range ordering in YbI₃ is rather strong, while it is significantly weaker in YbCl₃. On the other hand, the broad hump due to short-range ordering is much more pronounced in YbCl₃ compared to YbI₃. If this broad hump is due to 2D spin correlations, as has been argued in the literature [31], we expect it to be more pronounced in YbI₃, where the interlayer separation is larger. This aspects should be looked into more carefully in the future studies. Another notable difference in the heat capacity of two compounds is that in YbCl₃, a weak sample dependent anomaly is reported at 0.4 K, which is absent in YbI₃.

Magnetic behavior of the two compounds above 2 K is qualitatively similar. Further low temperature measurements on YbI₃ might prove useful in this context. The saturation moments $M_s^\parallel \approx 1.5 \mu_B/\text{Yb}^{3+}$ and $M_s^\perp \approx 1 \mu_B/\text{Yb}^{3+}$ is nearly the same for both the compounds. The differences may crop up at lower temperatures, hence, magnetic measurements below 2 K would be interesting.

In conclusion, YbI₃ possesses a more symmetric structure compared to YbCl₃, with C₃ symmetry preserved, similar to α -RuCl₃, whereas YbCl₃ exhibits broken C₃ symmetry. The nearest neighbor Yb–Yb separation along the *c*-axis is found to be larger in YbI₃ compared to YbCl₃. Heat capacity measurements show a similar two-step ordering for both compounds: initial short-range ordering followed by long-range antiferromagnetic ordering. Any further additional anomaly due to poor quality of the sample is absent in YbI₃. In the paramagnetic state ($T > 2$ K), the magnetic behavior of YbI₃ resembles that of YbCl₃.

IV. SUMMARY & CONCLUSIONS

To conclude, we have successfully grown high-quality single crystals of YbI_3 using a vapor transport reaction, taking elemental Yb and I as the starting precursors. The crystal field split ground state of Yb^{3+} in YbI_3 is a well-isolated Kramer's doublet with $g_J^\perp \approx 3.0 \pm 0.2$ (out-of-plane), and $g_J^\parallel \approx 3.4 \pm 0.3$ (in-plane). The in-plane isothermal magnetization shows weak a field induced transition, the indicating presence of slight anisotropy even within the *ab*-plane.

Heat capacity show a two-step magnetic transition with a broad peak $T_1 = 0.95$ K due to short-range correlations between the Yb moments, followed by a sharp peak at 0.6 K, signaling transition into a long-range magnetically ordered state. No additional anomaly, except an upturn below about 0.25 K due to nuclear Schottky effect, could be seen. The magnetic entropy, reaches almost 80% of $R \ln 2$ near 4 K (highest temperature in our experiment), consistent with the Kramer's doublet ground state. The value of critical exponent α of 2.5 from the heat capacity data suggests a possible unconventional

ground state for YbI_3 . To conclude, YbI_3 appears to harbor very interesting physics associated with $J_{\text{eff}} = 1/2$ on an ideal 2D honeycomb lattice. We believe that our preliminary study will trigger further experimental investigation to explore the spin Hamiltonian and exact ground state of this compound.

ACKNOWLEDGMENTS

The authors acknowledge UGC-DAE-CRS user facility for magnetization and low-temperature specific heat measurements. S.R. acknowledges I-HUB, National Mission on Interdisciplinary CyberPhysical Systems (NM-ICPS) of the Department of Science and Technology, Government of India, for the postdoctoral fellowship. L.H. and S.S. thank I-HUB (NM-ICPS) for partial financial support. S.S. thanks financial assistance received under the Scheme for Transformational and Advanced Research in Sciences (STARS) by the Ministry of Education, Government of India (sanction order no. STARS/APR2019/PS/358/FS). N.P. thanks Council for Scientific and Industrial Research (CSIR) for Ph.D. fellowship. P.T. thanks DST INSPIRE for the Ph.D. fellowship.

-
- [1] L. Savary and L. Balents, *Reports on Progress in Physics* **80**, 016502 (2016).
 - [2] L. Balents, *nature* **464**, 199 (2010).
 - [3] A. Kitaev, *Annals of Physics* **321**, 2 (2006), january Special Issue.
 - [4] G. Jackeli and G. Khaliullin, *Phys. Rev. Lett.* **102**, 017205 (2009).
 - [5] Y. Singh and P. Gegenwart, *Phys. Rev. B* **82**, 064412 (2010).
 - [6] X. Liu, T. Berlijn, W.-G. Yin, W. Ku, A. Tsvelik, Y.-J. Kim, H. Gretarsson, Y. Singh, P. Gegenwart, and J. P. Hill, *Phys. Rev. B* **83**, 220403 (2011).
 - [7] F. Ye, S. Chi, H. Cao, B. C. Chakoumakos, J. A. Fernandez-Baca, R. Custelcean, T. F. Qi, O. B. Korneta, and G. Cao, *Phys. Rev. B* **85**, 180403 (2012).
 - [8] Y. Singh, S. Manni, J. Reuther, T. Berlijn, R. Thomale, W. Ku, S. Trebst, and P. Gegenwart, *Phys. Rev. Lett.* **108**, 127203 (2012).
 - [9] S. C. Williams, R. D. Johnson, F. Freund, S. Choi, A. Jesche, I. Kimchi, S. Manni, A. Bombardi, P. Manuel, P. Gegenwart, and R. Coldea, *Phys. Rev. B* **93**, 195158 (2016).
 - [10] T. Takayama, A. Kato, R. Dinnebier, J. Nuss, H. Kono, L. S. I. Veiga, G. Fabbri, D. Haskel, and H. Takagi, *Phys. Rev. Lett.* **114**, 077202 (2015).
 - [11] A. Ruiz, A. Frano, N. P. Breznay, I. Kimchi, T. Helm, I. Oswald, J. Y. Chan, R. Birgeneau, Z. Islam, and J. G. Analytis, *Nature Communications* **8**, 961 (2017).
 - [12] A. Biffin, R. D. Johnson, I. Kimchi, R. Morris, A. Bombardi, J. G. Analytis, A. Vishwanath, and R. Coldea, *Phys. Rev. Lett.* **113**, 197201 (2014).
 - [13] K. Kitagawa, T. Takayama, Y. Matsumoto, A. Kato, R. Takano, Y. Kishimoto, S. Bette, R. Dinnebier, G. Jackeli, and H. Takagi, *Nature* **554**, 341 (2018).
 - [14] M. Abramchuk, C. Ozsoy-Keskinbora, J. W. Krizan, K. R. Metz, D. C. Bell, and F. Tafti, *Journal of the American Chemical Society* **139**, 15371 (2017).
 - [15] J. H. Roudebush, K. A. Ross, and R. J. Cava, *Dalton Trans.* **45**, 8783 (2016).
 - [16] V. Todorova, A. Leineweber, L. Kienle, V. Duppel, and M. Jansen, *Journal of Solid State Chemistry* **184**, 1112 (2011).
 - [17] K. W. Plumb, J. P. Clancy, L. J. Sandilands, V. V. Shankar, Y. F. Hu, K. S. Burch, H.-Y. Kee, and Y.-J. Kim, *Phys. Rev. B* **90**, 041112 (2014).
 - [18] R. D. Johnson, S. C. Williams, A. A. Haghighirad, J. Singleton, V. Zapf, P. Manuel, I. I. Mazin, Y. Li, H. O. Jeschke, R. Valentí, and R. Coldea, *Phys. Rev. B* **92**, 235119 (2015).
 - [19] J. Nasu, J. Knolle, D. L. Kovrizhin, Y. Motome, and R. Moessner, *Nature Physics* **12**, 912 (2016).
 - [20] L. J. Sandilands, Y. Tian, K. W. Plumb, Y.-J. Kim, and K. S. Burch, *Phys. Rev. Lett.* **114**, 147201 (2015).
 - [21] H. B. Cao, A. Banerjee, J.-Q. Yan, C. A. Bridges, M. D. Lumsden, D. G. Mandrus, D. A. Tennant, B. C. Chakoumakos, and S. E. Nagler, *Phys. Rev. B* **93**, 134423 (2016).
 - [22] A. Banerjee, J. Yan, J. Knolle, C. A. Bridges, M. B. Stone, M. D. Lumsden, D. G. Mandrus, D. A. Tennant, R. Moessner, and S. E. Nagler, *Science* **356**, 1055 (2017), <https://www.science.org/doi/pdf/10.1126/science.aah6015>.
 - [23] J. Bruin, R. Claus, Y. Matsumoto, N. Kurita, H. Tanaka, and H. Takagi, *Nature Physics* **18**, 401 (2022).
 - [24] F.-Y. Li, Y.-D. Li, Y. Yu, A. Paramekanti, and G. Chen, *Phys. Rev. B* **95**, 085132 (2017).
 - [25] J. G. Rau and M. J. P. Gingras, *Phys. Rev. B* **98**, 054408 (2018).
 - [26] S.-H. Jang, R. Sano, Y. Kato, and Y. Motome, *Phys. Rev. B* **99**, 241106 (2019).
 - [27] Y. Motome, R. Sano, S. Jang, Y. Sugita, and Y. Kato, *Journal of Physics: Condensed Matter* **32**, 404001 (2020).
 - [28] J. Xing, E. Feng, Y. Liu, E. Emmanouilidou, C. Hu, J. Liu, D. Graf, A. P. Ramirez, G. Chen, H. Cao, and N. Ni, *Phys. Rev. B* **102**, 014427 (2020).
 - [29] G. Sala, M. B. Stone, B. K. Rai, A. F. May, D. S. Parker, G. B. Halász, Y. Q. Cheng, G. Ehlers, V. O. Garlea, Q. Zhang, M. D.

- Lumsden, and A. D. Christianson, *Phys. Rev. B* **100**, 180406 (2019).
- [30] Y. Hao, H. Wo, Y. Gu, X. Zhang, Y. Gu, S. Zheng, Y. Zhao, G. Xu, J. W. Lynn, K. Nakajima, *et al.*, *Science China Physics, Mechanics & Astronomy* **64**, 1 (2021).
- [31] G. Sala, M. B. Stone, B. K. Rai, A. F. May, P. Laurell, V. O. Garlea, N. P. Butch, M. D. Lumsden, G. Ehlers, G. Pokharel, *et al.*, *Nature communications* **12**, 171 (2021).
- [32] Y. Matsumoto, S. Schnierer, J. A. Bruin, J. Nuss, P. Reiss, G. Jackeli, K. Kitagawa, and H. Takagi, *Nature Physics*, 1 (2024).
- [33] C. Wessler, B. Roessli, K. W. Krämer, B. Delley, O. Waldmann, L. Keller, D. Cheptikov, H. B. Braun, and M. Kenzelmann, *npj quantum materials* **5**, 85 (2020).
- [34] Agilent Technologies UK, CrysAlisPRO Software (Yarnton, England, 2014).
- [35] V. Petříček, M. Dušek, and L. Palatinus, *Zeitschrift für Kristallographie - Crystalline Materials* **229**, 345 (2014).
- [36] See Supplemental Material at [URL will be inserted by publisher] for details of the SEM - EDX analysis.
- [37] L. Asprey, T. Keenan, and F. Kruse, *Inorganic Chemistry* **3**, 1137 (1964).
- [38] Y. Kubota, H. Tanaka, T. Ono, Y. Narumi, and K. Kindo, *Phys. Rev. B* **91**, 094422 (2015).
- [39] S.-H. Do, S.-Y. Park, J. Yoshitake, J. Nasu, Y. Motome, Y. S. Kwon, D. Adroja, D. Voneshen, K. Kim, T.-H. Jang, *et al.*, *Nature Physics* **13**, 1079 (2017).
- [40] S. Kim, E. Horsley, J. P. C. Ruff, B. D. Moreno, and Y.-J. Kim, *Phys. Rev. B* **109**, L140101 (2024).
- [41] S. Park, S. Do, K.-Y. Choi, D. Jang, T. Jang, J. Schefer, C.-M. Wu, J. S. Gardner, S. Park, J.-H. Park, *et al.*, *Journal of Physics: Condensed Matter* (2024).
- [42] R. Yadav, N. A. Bogdanov, V. M. Katukuri, S. Nishimoto, J. Van Den Brink, and L. Hozoi, *Scientific reports* **6**, 37925 (2016).
- [43] M. T. Vandenborre, E. Husson, J. P. Chatry, and D. Michel, *Journal of Raman Spectroscopy* **14**, 63 (1983).
- [44] C.-T. Kuo, M. Neumann, K. Balamurugan, H. J. Park, S. Kang, H. W. Shiu, J. H. Kang, B. H. Hong, M. Han, T. W. Noh, and J.-G. Park, *Scientific Reports* **6**, 20904 (2016).
- [45] A. Chrissanthopoulos, G. D. Zissi, and G. N. Papatheodorou, *Zeitschrift für Naturforschung A* **60**, 739 (2005).
- [46] A. M. Hallas, J. Gaudet, N. P. Butch, M. Tachibana, R. S. Freitas, G. M. Luke, C. R. Wiebe, and B. D. Gaulin, *Phys. Rev. B* **93**, 100403 (2016).
- [47] A. Steppke, M. Brando, N. Oeschler, C. Krellner, C. Geibel, and F. Steglich, *physica status solidi (b)* **247**, 737 (2010), <https://onlinelibrary.wiley.com/doi/pdf/10.1002/pssb.200983062>.
- [48] Y. Ran, M. Hermele, P. A. Lee, and X.-G. Wen, *Phys. Rev. Lett.* **98**, 117205 (2007).